Journal of Magnetism and Magnetic Materials 637 (2026) 173681

Contents lists available at ScienceDirect

Journal of Magnetism and Magnetic Materials

journal homepage: www.elsevier.com/locate/jmmm

Magnetoimpedance properties of CoNbZr, multilayer CoNbZr/Au and multilayer NiFe/Au thin films

Indujan Sivanesarajah [a,*], Leon Abelmann [b], Uwe Hartmann [a]

[a] Institute of Experimental Physics, Saarland University, D-66041 Saarbrücken, Germany
[b] Department of Microelectronics, Delft University of Technology, 2600 AA Delft, The Netherlands

ARTICLE INFO

Keywords:
Amorphous CoNbZr thin films
Crystalline NiFe thin films
Au interlayer
Ferromagnetic resonance
Magnetoimpedance

ABSTRACT

Thin-film giant magnetoimpedance (GMI) structures are promising candidates for high-frequency magnetic sensing, with their performance governed by the interplay of electronic transport, magnetic softness, and ferromagnetic resonance (FMR). Optimisation therefore requires a comprehensive understanding of the properties of soft magnetic materials. This study investigates the structural, electric, magnetic, and GMI properties of sputtered amorphous CoNbZr single layers, amorphous CoNbZr/Au multilayers, and crystalline NiFe/Au multilayers. GMI measurements reveal distinct FMR frequencies of 1.4 GHz (CoNbZr), 0.7 GHz (CoNbZr/Au), and 0.5 GHz (NiFe/Au). Introducing Au interlayers into CoNbZr lowers the FMR frequency by 50% and enhances the maximum GMI ratio by a comparable margin relative to the single-layer film. At 1.8 GHz, the highest GMI performance is observed in a 20 μm × 5000 μm CoNbZr/Au strip, yielding 300% with a sensitivity of 249%/kAm^{-1}. Under identical conditions, single-layer CoNbZr reaches 180% (169%/kAm^{-1}) and NiFe/Au 280% (183%/kAm^{-1}), confirming the superior response of the CoNbZr/Au multilayer. These improvements are attributed to differences in in-plane demagnetising factors and saturation magnetisations, providing design guidelines for the development of resonant GHz-range GMI sensors.

1. Introduction

The giant magnetoimpedance (GMI) effect, characterised by a substantial change in the electrical impedance of soft magnetic materials under an applied magnetic field, has attracted significant interest due to its potential for magnetic field sensing [1–5]. GMI sensors have been explored in a wide range of applications, including the detection of biomagnetic fields [6–10]. In industrial non-destructive testing, GMI-based devices are used to detect magnetic contaminants and material defects [11], and they are also being considered for applications in the automotive sector [12].

Central to the GMI response are the magnetic materials employed. Soft magnetic alloys such as Permalloy ($Ni_{80}Fe_{20}$) and amorphous CoNbZr have become standard choices due to their high permeability, low coercivity, negligible magnetocrystalline anisotropy, and minimal magnetostriction [13,14]. Magnetocrystalline anisotropy originates from spin–orbit coupling, which links the direction of magnetisation to specific crystallographic axes. In Permalloy, the near-cubic symmetry of the NiFe lattice combined with the specific 80:20 composition minimises this anisotropy [15,16]. In contrast, in amorphous materials the absence of long-range atomic order suppresses preferred directions, resulting in negligible magnetocrystalline anisotropy as well.

Permalloy exhibits magnetic softness up to a critical thickness of approximately 150 nm to 200 nm [13,17,18], above which stress and/or columnar growth cause a perpendicular component in anisotropy and an increase in coercivity. Amorphous CoNbZr on the other hand maintains its favourable magnetic characteristics even at thicknesses exceeding 1 μm [14]. To overcome the thickness limitation of NiFe and preserve its magnetic softness at larger thicknesses, multilayer architectures incorporating thin metallic interlayers (e.g., Au, Cu, Ti, Ta, Cr) were independently proposed in 2004 [19,20]. These interlayers suppress columnar growth and help maintain soft magnetic properties, thereby extending the effective ferromagnetic thickness [21–25].

Several studies have explored specific parameters influencing the GMI performance of CoNbZr structures, including the orientation of the easy axis [26], element shape and aspect ratio [27], driving power [28], layout configurations (parallel versus meander) [29], Joule heating [30], and control of anisotropy direction during deposition [31]. These studies provide valuable insights into device-level

* Corresponding author.
E-mail address: sivanesa@outlook.de (I. Sivanesarajah).

https://doi.org/10.1016/j.jmmm.2025.173681
Received 15 May 2025; Received in revised form 2 November 2025; Accepted 12 November 2025
Available online 20 November 2025

optimisation but typically focus on isolated effects within specific configurations.

NiFe-based multilayers have been widely studied to assess the impact of lateral geometry on GMI. The interplay between induced transverse and longitudinal shape anisotropies enhances transverse permeability [32]. Ferromagnetic resonance (FMR) complements magnetisation measurements by characterising dynamic properties and resonance behaviour, with studies demonstrating the influence of multilayer architecture [33], reproducibility of broadband FMR fingerprints [34], and quantification of anisotropy and inhomogeneity [35]. Together, these works provide an established framework for interpreting GMI responses in NiFe systems.

Multilayer systems comprising amorphous/metallic interfaces [25,36–38], as well as those using SiO_2 interlayers [14,36,39,40], have been extensively investigated for their ability to enhance GMI performance. These architectures improve the AC permeability through magnetostatic coupling between adjacent magnetic layers across non-magnetic interlayers, thus modifying the dynamic magnetic response [14,36,39–41].

Despite these advances, a systematic comparison between NiFe and CoNbZr multilayers has not yet been reported. This study addresses this gap by investigating the magnetoimpedance properties of RF-sputtered CoNbZr single-layer films and multilayer stacks based on CoNbZr and NiFe. The comparative analysis includes structural, electric, and magnetic characterisation to evaluate their combined influence on the GMI response. Gold was selected as the interlayer material due to its high chemical stability and proof-of-concept suitability for multilayer fabrication [42]. The findings of this work aim to assess the viability of CoNbZr multilayers as a competitive alternative to the standard NiFe-based systems and to identify material design strategies for future miniaturised sensor applications.

2. Theory

This section presents the theoretical background necessary to understand the experimental results. First, the principles of magnetoimpedance is discussed, followed by an overview of theoretical models used in this study. Finally, the influence of the demagnetising field on the system is considered.

2.1. Magnetoimpedance

When an alternating current (AC) with frequency f flows through a soft magnetic conductor, the current distribution is influenced by the skin effect, causing the current density to decay exponentially from the surface. The characteristic skin depth δ depends on the vacuum permeability μ_0, the material's resistivity ρ, and its transverse permeability μ_t, which describes the material's response to the AC magnetic field generated by the current [43,44]:

$$\delta = \sqrt{\frac{\rho}{\pi f \mu_0 \mu_t}}. \tag{1}$$

The impedance $Z = R + iX$, with R the resistance and X the reactance, becomes dependent on the applied magnetic field through μ_t, directly linking the GMI response to the magnetic properties of the material.

For thin films (lateral dimensions $\gg 2t$), where t denotes the film thickness, the field- and frequency-dependent impedance can be modelled as [45,46]:

$$Z(H) = R_{DC}\, ikt \coth(ikt), \tag{2}$$

where R_{DC} is the DC resistance, and $k = (1+i)/\delta$ the propagation constant.

The giant magnetoimpedance response is characterised by the relative impedance change

$$\eta(H) = \frac{|Z(H)| - |Z(H_{ref})|}{|Z(H_{ref})|}, \tag{3}$$

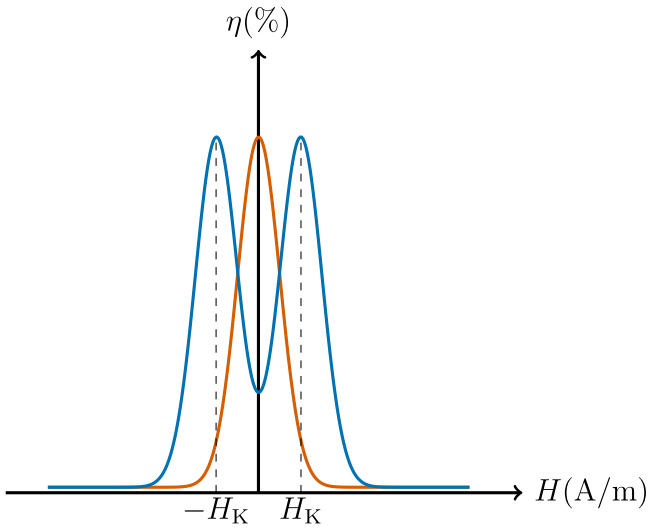

Fig. 1. Schematic representation of the GMI response as a function of the external field H, for different orientations of the magnetic easy axis relative to the AC current and applied field. For longitudinal anisotropy (red), with the easy axis parallel to the current and field, the GMI ratio η reaches its maximum at $H = 0$. For transverse anisotropy (blue), with the easy axis perpendicular to the current and field, the maximum occurs at the anisotropy field $\pm H_K$, resulting in a symmetric double-peak profile [13].

where H_{ref} is the reference magnetic field, corresponding to the maximum achievable field in the experiment at which the material is magnetically saturated.

By measuring $|Z|$ and its phase $\arg(Z)$, R and X are determined. The real, imaginary, and absolute components of k, δ, and μ_t are then extracted by numerically fitting Eq. (2) using the Levenberg–Marquardt (L-M) method [47,48].

The mechanisms underlying the GMI effect depend on the AC frequency. At low frequencies (up to a few kHz), impedance variations are dominated by the magnetoinductive effect [49]. In the intermediate range (100 kHz–a few MHz), the skin effect governs the impedance, with both domain wall motion and magnetisation rotation contributing to μ_t. At high frequencies (MHz–GHz), ferromagnetic resonance (FMR) and gyromagnetic effects dominate, controlling the variation in skin depth and thus the overall GMI response [46].

Fig. 1 illustrates the GMI response as a function of the sample's anisotropy axis orientation, with the AC current and applied field collinear. For the red curve, the magnetic easy axis is parallel to the current and field (longitudinal anisotropy), resulting in a single peak. The transverse permeability μ_t is maximal at $H = 0$ and decreases with increasing field until the material is saturated. Consequently, the GMI ratio is highest at zero field and vanishes at saturation [13].

For the blue curve, the magnetic easy axis is perpendicular to the current and field (transverse anisotropy). In this case, a symmetric double-peak profile appears, with μ_t reaching its maximum at the anisotropy field [13]:

$$H_K = \frac{2K_{eff}}{\mu_0 M_s}. \tag{4}$$

The sensitivity s of the GMI effect is calculated using the slope of the GMI curve [13]:

$$s = \frac{d\eta}{dH}. \tag{5}$$

These relations provide the theoretical basis for interpreting the shape of the GMI curves and for quantifying the sensor performance in terms of sensitivity.

2.2. Theoretical models

This section presents the theoretical models used to describe the electric resistivity and saturation magnetisation in multilayer systems. First, electric models are discussed, focusing on the parallel resistor model and dilution models, which are used to calculate resistivity in ferromagnetic and non-ferromagnetic layers. Then, magnetic models are introduced, where the dilution model is applied to estimate the saturation magnetisation in multilayer systems.

2.2.1. Electric models

The resistivity of ferromagnetic (FM) and non-ferromagnetic (NFM) layers within a multilayer system, consisting of N FM layers and $(N-1)$ NFM layers, can be determined from the measured resistance using a parallel resistor model. The total measured resistance, R, is given by [50]:

$$\frac{1}{R} = \frac{N-1}{R_{\mathrm{NFM}}} + \frac{N}{R_{\mathrm{FM}}}, \tag{6}$$

where R_{NFM} and R_{FM} are the resistances of the NFM and FM layers, respectively. From this relationship, the resistivities ρ_{NFM} and ρ_{FM} of the NFM and FM layers can be derived as:

$$\rho_{\mathrm{NFM}} = \frac{(N-1)t_{\mathrm{NFM}} w\, \rho_{\mathrm{FM}} R}{\rho_{\mathrm{FM}} l - N t_{\mathrm{FM}} w R}, \tag{7}$$

$$\rho_{\mathrm{FM}} = \frac{N t_{\mathrm{FM}} w\, \rho_{\mathrm{NFM}} R}{\rho_{\mathrm{NFM}} l - (N-1) t_{\mathrm{NFM}} w R}, \tag{8}$$

where ρ_{NFM} and ρ_{FM} are the resistivities, and t_{NFM} and t_{FM} are the thicknesses of the NFM and FM layers, respectively. Here, w represents the width, and l represents the length of the layers.

A complementary approach is the dilution model, which estimates the effective resistivity based on the volumetric ratio of FM and NFM layers. This model assumes that the NFM layers have a negligible impact on the total resistivity, allowing the resistivity of the multilayer system to be approximated primarily by the FM layers. The generalised expression for the resistivity, ρ'_{layer}, in both single-layer and multilayer films is:

$$\rho'_{\mathrm{layer}} = \frac{t_{\mathrm{layer,tot}}}{t_{\mathrm{tot}}} \rho_{\mathrm{layer}}, \tag{9}$$

where $t_{\mathrm{layer,tot}}$ is the total thickness of the FM or NFM layers being considered, t_{tot} is the total thickness of the entire film, and ρ_{layer} is the measured resistivity of the FM or NFM layer.

For a single-layer system, where $t_{\mathrm{layer,tot}} = t_{\mathrm{tot}}$, Eq. (9) reduces to $\rho'_{\mathrm{layer}} = \rho_{\mathrm{layer}}$, indicating that the measured resistivity corresponds directly to the intrinsic resistivity of the layer.

2.2.2. Magnetic models

The saturation magnetisation $M_{\mathrm{s,FM}}$ of the FM layer can be used to estimate the effective saturation magnetisation of a multilayer system by applying a dilution model based on the FM volume fraction. Assuming that the NFM layers have a negligible influence on the saturation magnetisation, the saturation magnetisation $M'_{\mathrm{s,layer}}$ of the multilayer system can be calculated using the ratio of the total thickness $t_{\mathrm{FM,tot}}$ of the FM layers to the total thickness t_{tot} of the entire film:

$$M'_{\mathrm{s,layer}} = \frac{t_{\mathrm{FM,tot}}}{t_{\mathrm{tot}}} M_{\mathrm{s,FM}}. \tag{10}$$

2.3. Demagnetising field

Demagnetising factors quantify the reduction of the internal magnetic field due to the sample geometry [51,52]. For rectangular thin films, the demagnetising factors (N_x, N_y, N_z) depend on the aspect ratio of the sample dimensions (length l, width w, thickness t) and are essential for describing shape anisotropy and its contribution to the effective anisotropy field. In the thin-film limit, the out-of-plane factor N_z approaches unity, while the in-plane factors N_x and N_y remain small but determine the effective in-plane anisotropy. The analytical closed-form expressions for the demagnetising factors of rectangular prisms were derived by Aharoni [52]. In this formulation, the half-dimensions are defined as $a = w/2$, $b = t/2$, and $c = l/2$. For N_x one obtains [52]:

$$\begin{aligned}
\pi N_x = {} & \frac{b^2-c^2}{2bc} \ln\left(\frac{\sqrt{a^2+b^2+c^2}-a}{\sqrt{a^2+b^2+c^2}+a}\right) \\
& + \frac{a^2-c^2}{2ac} \ln\left(\frac{\sqrt{a^2+b^2+c^2}-b}{\sqrt{a^2+b^2+c^2}+b}\right) \\
& + \frac{b}{2c} \ln\left(\frac{\sqrt{a^2+b^2}+a}{\sqrt{a^2+b^2}-a}\right) + \frac{a}{2c} \ln\left(\frac{\sqrt{a^2+b^2}+b}{\sqrt{a^2+b^2}-b}\right) \\
& + \frac{c}{2a} \ln\left(\frac{\sqrt{b^2+c^2}-b}{\sqrt{b^2+c^2}+b}\right) + \frac{c}{2b} \ln\left(\frac{\sqrt{a^2+c^2}-a}{\sqrt{a^2+c^2}+a}\right) \\
& + 2\arctan\left(\frac{ab}{c\sqrt{a^2+b^2+c^2}}\right) + \frac{a^3+b^3-2c^3}{3abc} \\
& + \frac{a^2+b^2-2c^2}{3abc}\sqrt{a^2+b^2+c^2} + \frac{c}{ab}\left(\sqrt{a^2+c^2}+\sqrt{b^2+c^2}\right) \\
& - \frac{(a^2+b^2)^{3/2}+(b^2+c^2)^{3/2}+(c^2+a^2)^{3/2}}{3abc}.
\end{aligned} \tag{11}$$

The corresponding expression for N_y is obtained by interchanging a and c. These expressions assume uniform magnetisation and neglect the finite susceptibility of the material. This limitation can be addressed by the correction scheme proposed by Chen et al. [53], which introduces susceptibility-dependent factors into the demagnetising coefficients. The corresponding shape anisotropy constant K_{s} is expressed as [16]:

$$K_{\mathrm{s}} = \frac{1}{2}\mu_0 \left(N_y - N_x\right) M^2. \tag{12}$$

Table 1
Calculated in-plane demagnetising factors N_x and N_y (along the length and width, respectively) for rectangular single-layer (thickness t = 1040 nm) and multilayer (total thickness t = 1130 nm) films with varying lateral aspect ratios $l : w$, assuming M = 1 MA/m. For multilayers, the stack is treated as a homogeneous film with the given total dimensions, neglecting individual layer structure [52].

System	Single-layer		Multilayer	
$l : w$	N_x (10^{-4})	N_y (10^{-4})	N_x (10^{-4})	N_y (10^{-4})
1000:100	19	198	20	212
1000:50	17	352	18	377
500:20	27	731	29	780
1000:20	14	734	15	783
2000:20	7	736	7	784
1000:10	12	1243	12	1321
1000:5	9	2032	10	2149
5000:20	3	737	3	786

Table 1 summarises the calculated in-plane demagnetising factors for representative single-layer and multilayer structures investigated in this work. For multilayer stacks, the demagnetising factors were calculated by treating the system as an effective homogeneous body with the total dimensions of the stack (thickness, width, and length). This approximation neglects the internal stratification of the multilayer, assuming that demagnetising effects are dominated by the overall sample geometry rather than by the individual layers. While Aharoni's formalism strictly applies only to single-phase rectangular prisms, this approach provides a reasonable estimate of the in-plane demagnetising factors for the studied thin-film stacks.

The effects of demagnetising fields have been quantitatively discussed in previous works [53], highlighting the necessity of considering demagnetising fields when interpreting or simulating the GMI response in patterned ferromagnetic films.

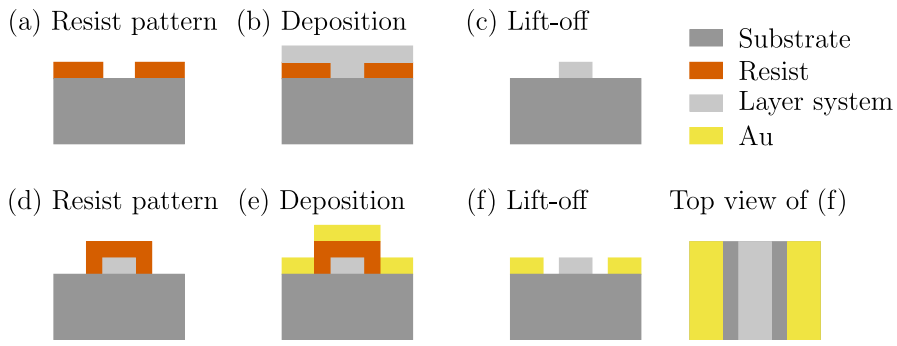

Fig. 2. Schematic representation of the sample preparation process. The steps include patterning the photoresist (a,d), depositing the layer system (b) and gold (e), and removing the photoresist via lift-off (c,f).

Table 2
Parameters for sputter deposition (VSW technology).

Target composition (at.%)	Pressure 10^{-3} mbar	Power W	Rate nm/min
$Co_{85}Nb_{12}Zr_3$	1.7 ± 0.1	100 ± 2 RF	4.9 ± 0.2
$Ni_{81}Fe_{19}$	1.7 ± 0.1	85 ± 2 RF	4.9 ± 0.2
Au	5.0 ± 0.1	50 ± 1 DC	21.0 ± 0.2

3. Materials and methods

This section outlines the materials and methods used in this study, including sample fabrication, characterisation, and experimental setup.

3.1. Sample preparation

Fig. 2 illustrates the schematic representation of the sample preparation process. Si–SiO_2 (20 mm × 20 mm) samples were cleaned with acetone, isopropanol, and deionised water before spin-coating an adhesion promoter (AR 300-80, Allresist) at 4000 rpm for 1 min and baking at 180 °C for 2 min. Subsequently, the positive photoresist (AR-P 5320, Allresist) was spin-coated for 1 min at 4000 rpm and baked for 4 min at 105 °C.

The samples were patterned into stripes with widths ranging from 5 µm to 100 µm and lengths from 0.5 mm to 5 mm using laser lithography (µPG 101, Heidelberg Instruments). After development in AR 300-26 (Allresist) for 3 min, rinsing with deionised water, and drying with nitrogen, the patterned substrates were mounted on a rotating holder at a target-to-substrate distance of 12 cm. Once the base pressure had decreased below $1 \cdot 10^{-8}$ mbar, the layer systems shown in Fig. 3 were deposited using the sputtering parameters summarised in Table 2.

The Au interlayers were deposited with a constant thickness of 10 nm to ensure electric continuity in sputtered films [54] and to enable a direct comparison between CoNbZr/Au and NiFe/Au systems. After the lift-off process, contact pads for the RF probes (FPC-GSG-150, Cascade Microtech) were patterned onto the stripes, followed by Au sputtering under the same conditions (Table 2) and a second lift-off step.

The fabricated samples are shown in Fig. 4, including the Au patterns used for resistance measurements (Fig. 4(a)) and for magnetoimpedance measurements (Fig. 4(b)).

3.2. Microstructural characterisation

The electron diffraction patterns were acquired using a JEOL ARM-200F TEM equipped with a LaB_6 cathode and operated at 200 kV. For this purpose, TEM slices were prepared by milling an area of 15 µm × 5 µm out of a continuous film using a focused-ion beam (FIB) and an in situ lift-off with a micromanipulator [55]. The elemental composition of the TEM slices was determined using an EDAX energy dispersive X-ray spectroscopy (EDX) system.

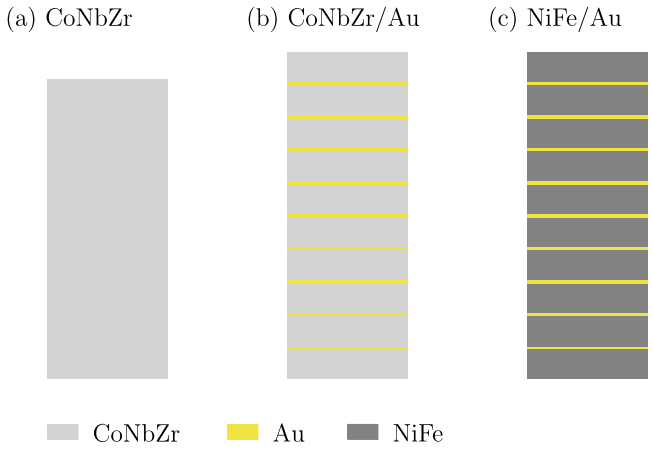

Fig. 3. Schematic representation of the layer systems in cross-section: (a) a single-layer CoNbZr system with a film thickness of 1040 nm; (b) a multilayer system consisting of 10 layers of CoNbZr and 9 layers of Au, with individual film thicknesses of 104 nm and 10 nm, respectively; and (c) a multilayer system composed of 10 layers of NiFe and 9 layers of Au, with the same respective thicknesses of 104 nm and 10 nm.

3.3. Magnetic characterisation

For the magnetic measurements, the in-plane hysteresis loops of one patterned stripe (0.1 mm × 1 mm) on 8 mm × 8 mm samples were measured by a Vibrating Sample Magnetometer (PPMS-VSM, Quantum Design). The system was calibrated using a 0.25 g Pd cylinder with a known magnetic moment of 0.013 mAm^2 at 1 T and 298 K based on the literature value of the mass susceptibility of Pd ($5.25 \cdot 10^{-2}$ Am^2/kg [56]. The diamagnetic contribution of sample holder and Si substrate was subtracted as a linear background signal of 0.1 $\mu Am^2/T$, obtained from a fit to the high-field branches of the in-plane hysteresis loops. Additionally, magneto-optic Kerr effect (MOKE) images were taken to observe the domain structures.

3.4. Experimental setup

Fig. 5 shows the setups used for resistance and magnetoimpedance measurements. In Fig. 5(a), a Source Measure Unit (SMU; B2901A, Keysight) is used to determine the resistance using the four-probe method. The samples with the lateral dimensions of 0.1 mm × 1 mm are contacted using two RF probes and are connected in series to the SMU. The voltage U is measured over a defined length of 0.45 mm. The SMU is controlled by a PC via LAN.

For GMI measurements, as shown in Fig. 5(b), the samples were placed in the centre of a pair of Helmholtz coils operated by a programmable unipolar current source (Hercules 2500 (250 V, 10 A), TET

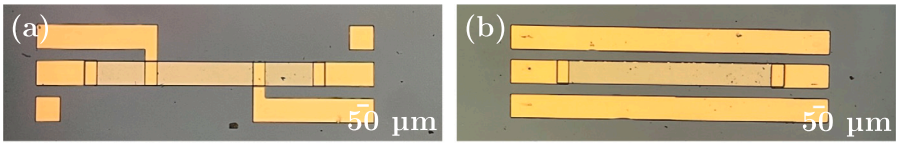

Fig. 4. Images of the patterns used for (a) resistance and (b) magnetoimpedance measurements.

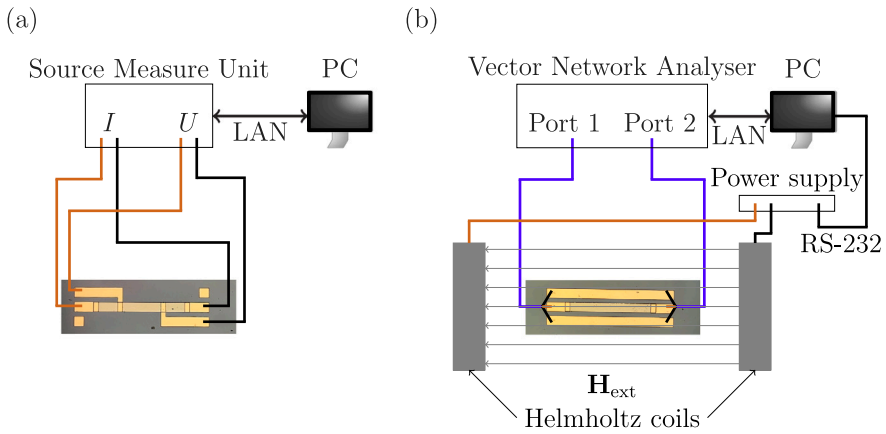

Fig. 5. Schematic setup used for (a) resistance and (b) magnetoimpedance measurements.

Electronics). The current source is connected to the PC via a RS-232 USB converter. A maximum current of 10 A (corresponding to H_{ext} = 32 kA/m) was used to generate the external magnetic field, and polarity was manually reversed via a changeover switch. This magnetic field was used as the reference field for calculating the GMI ratio.

High-frequency measurements were performed using a vector network analyser (VNA; ZNL3, Rohde & Schwarz) connected to RF probes via coaxial cables. The test structures were designed in coplanar waveguide (CPW) configuration to reduce the parasitic contributions of the measurement environment. CPWs are well suited for thin-film structures due to their planar layout, reduced parasitic loading, and improved impedance matching [57].

A full two-port calibration was performed using the Thru-Open-Short-Match (TOSM) procedure on a standard impedance substrate (101–190C, Cascade Microtech). This defines the reference plane directly at the probe tips and eliminates systematic errors originating from the measurement cables, connectors, and probes.

To obtain the intrinsic impedance of the device under test (DUT), parasitic effects introduced by the measurement fixture such as pads, interconnects, and probe coupling must be removed. For this purpose, dedicated de-embedding structures were designed following the methodology described in [58,59]. These included open-circuit and short-circuit configurations with identical coplanar waveguide (CPW) geometry and layout as the DUT (see Fig. 6), used to capture parasitic admittances and impedances, respectively.

Their geometry was carefully matched to the DUT in terms of signal width, gap size, pad dimensions, and CPW length to ensure identical high-frequency behaviour. This procedure ensures that the extracted impedance corresponds solely to the thin-film stack, excluding any contributions from the measurement environment.

The frequency response of the DUT and reference structures was measured over a frequency range from 1 MHz to 3 GHz in 1 MHz steps with a bandwidth of 1 kHz and an output power of −20 dBm (10 µW). The measurements were recorded separately for each RF probe and stored on the VNA for post-processing, including de-embedding and impedance extraction.

The experimental setup for heat treatment of the GMI structures is illustrated in Fig. 7. The structures were contacted with two RF probes and connected in series with the SMU via banana cables, which were linked to the RF probes through SMA-BNC adapters and BNC-banana connectors. Joule heating and the associated Oersted field induced magnetic anisotropy. Constant current was applied for 1 min in ambient air, following [60].

4. Results and discussion

This section presents the results and discusses the key findings of the study with respect to the magnetoimpedance behaviour of the investigated systems. The microstructural, electric, and magnetic properties are first analysed in order to understand their individual and combined impact on the GMI response. Finally, the findings are discussed in relation to the underlying mechanisms and their relevance for the design of high-performance multilayer sensors.

4.1. Microstructural and compositional analysis

The microstructural properties of the deposited thin films were analysed by TEM, selected area electron diffraction (SAED), and EDX, as shown in Fig. 8. Diffraction spot and ring distances were averaged over five measurements per sample for robust analysis. Line profiles were then extracted from the diffraction rings to identify the corresponding crystallographic planes. Average values were calculated, and the standard deviation was used to determine the uncertainty in the interplanar spacings.

The single-layer CoNbZr film (Fig. 8(a)–(c)) exhibits a homogeneous and featureless cross-section (Fig. 8(a), (b)), consistent with an amorphous structure, further supported by the diffuse ring in the SAED pattern (Fig. 8(c)). The appearance of a faint second ring in the pattern is attributed to instrumental artefacts.

In the CoNbZr/Au system (Fig. 8(d)–(f)), the TEM cross-sections reveal well-defined alternating layers of amorphous CoNbZr and crystalline Au. The amorphous nature of the CoNbZr layers is indicated by the diffuse background in the SAED pattern (Fig. 8(f)), while the sharp diffraction spots correspond to the crystalline Au layers. These features are consistent with the cross-sectional images (Fig. 8(e)), in which Au grains can be clearly identified. The measured interplanar spacings of the diffraction spots were $d = (0.237 \pm 0.001)$ nm, (0.118 ± 0.001) nm, and

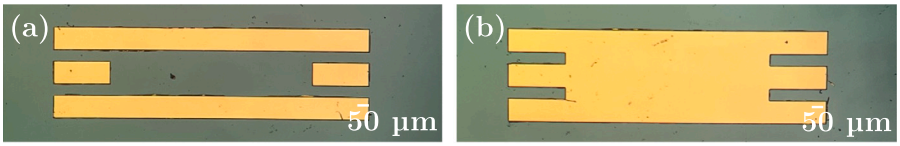

Fig. 6. De-embedding structures used for magnetoimpedance measurements containing (a) open and (b) short structures.

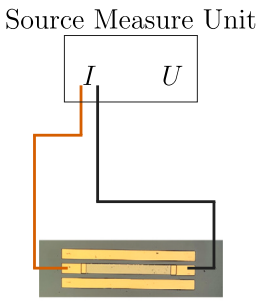

Fig. 7. Schematic setup used for annealing the GMI structures.

Table 3
Elemental composition (at.%) of the targets and sputtered films for the CoNbZr and NiFe systems. The target compositions were optimised for near-zero magnetostriction (<1 ppm) [63,64].

Element	Co	Nb	Zr	Ni	Fe
Target (at.%)	85 ± 1	12 ± 1	3 ± 1	81 ± 1	19 ± 1
Film (at.%)	90 ± 1	8 ± 1	2 ± 1	80 ± 1	20 ± 1

(0.080 ± 0.001) nm. Using the lattice constant of Au ($a = 0.409$ nm [61]) and the relation $d = a/\sqrt{h^2 + k^2 + l^2}$, these values were assigned to the (111), (222), and (333) planes, respectively. The presence of sharp interfaces between CoNbZr and Au suggests minimal interdiffusion, indicating a well-controlled sputtering process.

The NiFe/Au multilayer (Fig. 8(g)–(i)) also exhibits clearly defined, alternating layers. The NiFe layers display grain-like features, indicative of crystallinity, while the Au layers remain polycrystalline. The SAED pattern (Fig. 8(i)) shows multiple diffraction rings with discrete spots. Using the lattice constant of $Ni_{80}Fe_{20}$ ($a = 0.355$ nm [62]), the measured d-spacings were assigned to the (111), (200), (220), and (222) planes, corresponding to (0.206 ± 0.001) nm, (0.178 ± 0.001) nm, (0.126 ± 0.001) nm, and (0.107 ± 0.001) nm, respectively. A fifth diffraction ring corresponds to the (333) plane of Au, confirming the crystalline character of both constituents in the multilayer stack.

Two faint artefacts at approximately 1 and 7 o'clock were observed in all SAED patterns (Fig. 8(c), (f), (i)). As their positions remained unchanged under sample rotation and varying imaging conditions, these features are attributed to instrumental effects rather than structural characteristics and do not affect the interpretation of the crystalline order.

The elemental compositions determined by EDX (Table 3) reveal a pronounced increase in the Co/Nb ratio in the sputtered film compared to the target material (from 7 to 11). This deviation likely arises from differences in the sputtering yields or deposition rates of Co and Nb. Contributing factors include disparities in atomic mass and radius, as well as process-dependent parameters such as chamber pressure and target-to-substrate distance [65]. In particular, the sputtering yield of Nb is reported to be approximately half that of Co under comparable conditions, which promotes a preferential incorporation of Co into the growing film [66].

Such an enrichment of Co can significantly influence the magnetic and magnetoimpedance properties of the resulting film, as both saturation magnetisation and magnetic permeability are strongly composition-dependent [67]. These findings underscore the need for precise composition control when designing multilayer structures for optimal GMI performance.

Table 4
Comparison of the measured and calculated resistivities (ρ) for the sputtered films. The resistivities of Au and NiFe were extracted using the parallel resistor model (Eqs. (6), (7), and (8)).

Film	CoNbZr	CoNbZr/Au	NiFe/Au	Au	NiFe
ρ (µΩ cm)	119 ± 4	71 ± 3	26 ± 1	12 ± 4	29 ± 20
ρ' (µΩ cm)	119 ± 4	110 ± 12	27 ± 2	12 ± 4	29 ± 20

4.2. Electric properties

Table 4 provides an overview of both measured and calculated resistivities of the sputtered films. The amorphous CoNbZr single-layer exhibits a resistivity of (119 ± 4) µΩ cm, which is in good agreement with literature values reported for $Co_{85}Nb_{12}Zr_3$ [30]. The incorporation of Au leads to a significant reduction in the CoNbZr/Au multilayers to (71 ± 3) µΩ cm, whereas the multilayer NiFe/Au films exhibit resistivities as low as (26 ± 1) µΩ cm.

The resistivities of Au and NiFe were estimated using a parallel resistor model (Eqs. (7) and (8)). Initially, ρ_{CoNbZr} was used to calculate ρ_{Au}, which subsequently served as an input for the determination of ρ_{NiFe}. Due to the Au layer thickness being below the electron mean free path (37.7 nm [68]), the estimated resistivity for Au is approximately six times greater than its bulk value (2.214 µΩ cm [68]). Similarly, the derived NiFe resistivity exceeds the bulk value (22 µΩ cm [69]) by approximately 30%. The associated uncertainties primarily originate from uncertainties in layer thickness and lateral dimensions.

The large uncertainty in ρ_{Au}, estimated as $\Delta\rho_{Au} \approx \frac{1}{3}\rho_{Au}$, propagates into the error of ρ_{NiFe} and contributes to the comparatively large uncertainty of 70% relative to the extracted ρ_{NiFe} value. Still, the extracted resistivity value remains within the typical range for thin NiFe films.

Comparison with the dilution model (Eq. (9)) shows good agreement for the NiFe/Au system. In contrast, the calculated value for CoNbZr/Au exceeds the measured resistivity by approximately 55%, suggesting that the model may fail to fully capture microstructural influences and scattering mechanisms in amorphous multilayers. The reduced resistivity observed in CoNbZr/Au is likely to directly impact its GMI performance.

4.3. Magnetic properties

The in-plane hysteresis loops of the magnetisation M, measured for a field sweep of $B = \pm 30$ mT on patterned 0.1 mm × 1 mm elements of single-layer CoNbZr, multilayer CoNbZr/Au, and NiFe/Au in both the length and width directions are depicted in Fig. 9. The saturation magnetisations were estimated by taking the magnetic moment at the maximum applied field of 30 mT and normalising it to the volume of the sputtered stripes, accounting for the Au thickness in the calculation. This yielded values of (1.01 ± 0.05) MA/m for CoNbZr, which is 27% higher than the value reported for $Co_{85}Nb_{12}Zr_3$ [30]), (0.85 ± 0.04) MA/m for CoNbZr/Au, and (0.68 ± 0.03) MA/m for NiFe/Au. It should be noted that the CoNbZr sample is nearly saturated at the maximum applied field of 30 mT.

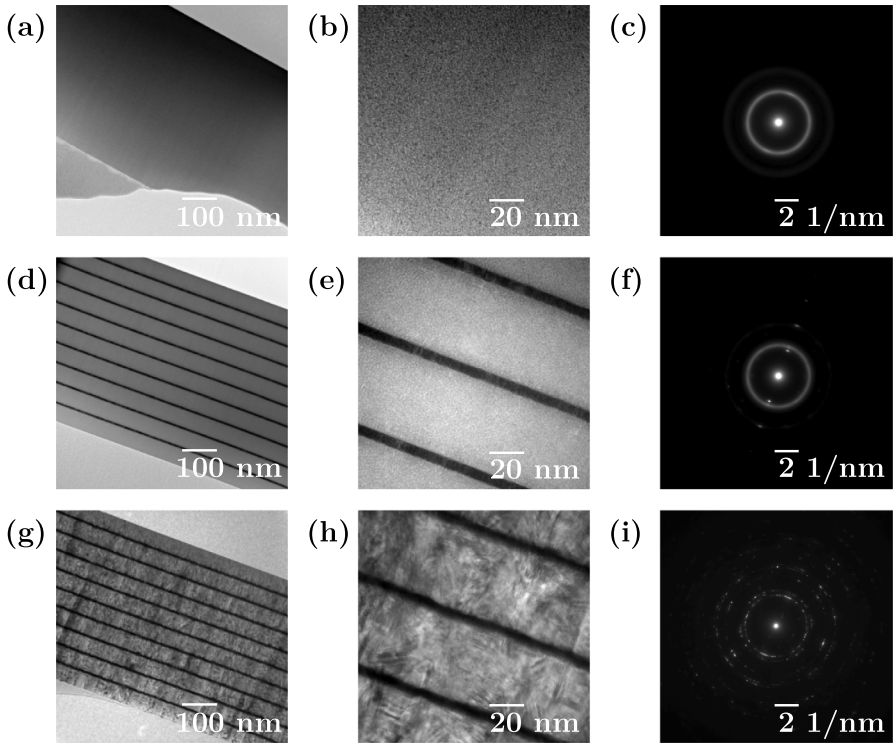

Fig. 8. Cross-sectional TEM images and SAED patterns of (a–c) single-layer CoNbZr, (d–f) multilayer CoNbZr/Au, and (g–i) multilayer NiFe/Au. The CoNbZr single layer shows a uniform amorphous structure with a diffuse SAED ring. In CoNbZr/Au, alternating amorphous and crystalline layers are observed, with Au diffraction spots. In NiFe/Au, both NiFe and Au layers are crystalline, as confirmed by the SAED patterns.

Table 5
Magnetic properties of CoNbZr, CoNbZr/Au, and NiFe/Au thin films: coercive field (B_c), remanent-to-saturation ratio (M_r/M_s), and maximum permeability (μ_{max}) for longitudinal and transverse directions.

Sample	Parameter	CoNbZr	CoNbZr/Au	NiFe/Au
In-plane (Length)	B_c (mT)	0.09 ± 0.01	5.11 ± 0.01	0.36 ± 0.01
	M_r/M_s	0.17 ± 0.01	0.80 ± 0.01	0.41 ± 0.01
	μ_{max} (10^3)	7.00 ± 0.10	1.20 ± 0.10	4.60 ± 0.10
Out-of-plane (Width)	B_c (mT)	4.86 ± 0.01	4.16 ± 0.01	4.20 ± 0.01
	M_r/M_s	0.61 ± 0.01	0.82 ± 0.01	0.37 ± 0.01
	μ_{max} (10^3)	0.8 ± 0.1	2.2 ± 0.1	1.7 ± 0.1

Table 6
Comparison of calculated saturation magnetisations considering either the total sputtered thickness of the films or only the magnetic layers. The estimates $M_{s,t_{tot}}$, based on the total thickness t_{tot}, indicate a reduction of 16% for CoNbZr/Au relative to CoNbZr, and 21% for NiFe/Au relative to the literature value for NiFe (0.86 MA/m [70]). The dilution model (Eq. (10)) reproduces the values for all three systems.

		CoNbZr	CoNbZr/Au	NiFe/Au
$M_{s,t_{tot}}$	(MA/m)	1.01 ± 0.05	0.85 ± 0.04	0.68 ± 0.03
$M_{s,t_{FM,tot}}$	(MA/m)	1.01 ± 0.05	0.92 ± 0.05	0.74 ± 0.04
M'_s	(MA/m)	1.01 ± 0.05	0.93 ± 0.12	0.79 ± 0.06

Based on Fig. 9, the coercive field (B_c), the remanent-to-saturation magnetisation ratio (M_r/M_s, with M_r denoting the magnetisation at zero applied field), and the maximum permeability (μ_{max}, defined as the maximum slope of the magnetisation curve) were extracted and are summarised in Table 5.

Along the length direction, the coercive field for CoNbZr is (0.09 ± 0.01) mT, which is 57 times lower than CoNbZr/Au ((5.11 ± 0.01) mT) and 4 times lower than NiFe/Au ((0.36 ± 0.01) mT). The maximum permeability for CoNbZr reaches approximately 7000, which is 6 times higher than CoNbZr/Au and 1.5 times higher than NiFe/Au. The remanent magnetisation to saturation magnetisation ratios are 0.17 for CoNbZr, 0.80 for CoNbZr/Au, and 0.41 for NiFe/Au. All samples exhibit distinct steps in their hysteresis loops along the length direction.

Along the width direction, the coercive field for CoNbZr is (4.86 ± 0.01) mT, which is 17% higher than CoNbZr/Au ((4.16 ± 0.01) mT) and 16% higher than NiFe/Au ((4.20 ± 0.01) mT). The maximum permeability for CoNbZr is around 800, which is 2.75 times lower than CoNbZr/Au and 2 times lower than NiFe/Au. The remanent magnetisation to saturation magnetisation ratios are 0.61 for CoNbZr, 0.82 for CoNbZr/Au, and 0.37 for NiFe/Au.

The hysteresis loops indicate that for single-layer CoNbZr and multilayer NiFe/Au, the magnetic easy axis lies in the length direction, as evidenced by significantly smaller coercive fields compared to the width direction. This effect is attributed to the lower demagnetising factor along the length direction (approximately 0.002 [52]), which is about an order of magnitude smaller than that in the width direction. However, no clear magnetic easy axis is observed for CoNbZr/Au, as the hysteresis loops for both directions appear similar.

Table 6 lists the calculated saturation magnetisations, considering both the total sputtered film thickness and the thickness of the magnetic layers only. The error results from the uncertainties of the film dimensions as well as the measurement of the magnetic moment m. The estimated saturation magnetisations $M_{s,t_{tot}}$ considering the total sputtered thickness t_{tot} reveal that CoNbZr/Au is 16% lower than CoNbZr, and NiFe/Au is 21% lower than the literature value for NiFe (0.86 MA/m [70]). Additionally, employing a dilution model (see Eq. (10)) reveals agreement for CoNbZr, CoNbZr/Au and NiFe/Au.

The measured magnetic properties reveal that the single-layer CoNbZr exhibits a relatively low maximum transverse permeability (800),

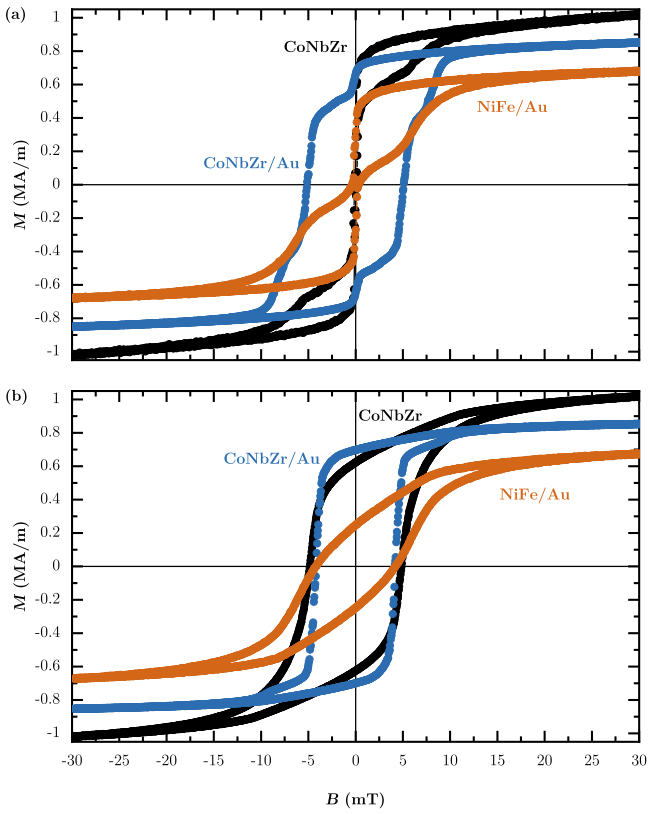

Fig. 9. In-plane hysteresis loops of $0.1\,\text{mm} \times 1\,\text{mm}$ patterned elements for CoNbZr, CoNbZr/Au, and NiFe/Au, measured along (a) longitudinal and (b) transverse directions.

which may limit its magnetoimpedance response. In contrast, the CoNbZr/Au multilayer shows a significantly increased transverse permeability (2200) despite a higher coercive field, indicating enhanced magnetic softness in the transverse direction that benefits GMI performance. The NiFe/Au multilayer presents intermediate coercivity and transverse permeability values, reflecting a balanced magnetic behaviour. Consequently, the enhanced transverse permeability in CoNbZr/Au is expected to improve its magnetoimpedance response, potentially compensating for the increased coercivity.

4.4. Magnetoimpedance analysis

This section examines the magnetoimpedance characteristics of the samples, focusing on the influence of critical parameters such as the applied magnetic field, frequency, annealing current, and lateral aspect ratio.

4.4.1. Influence of field and frequency

The GMI ratios η for $0.1\,\text{mm} \times 1\,\text{mm}$ elements as a function of frequency for single-layer CoNbZr, multilayer CoNbZr/Au, and multilayer NiFe/Au under a field sweep of $H = \pm 8\,\text{kA/m}$ are shown in Fig. 10. Across all systems, the GMI ratio increases with frequency due to the decreasing skin depth (Eq. (1)).

For single-layer CoNbZr (Fig. 10(a)), the GMI response initially exhibits a single peak. However, minor double peaks appear above 0.3 GHz, likely due to experimental misalignments. Beyond 1.4 GHz, the broadening of the GMI curves and the shift of the double peaks to higher fields mark the onset of the FMR regime. This observation aligns with Endo et al. [67], who reported an FMR frequency of 1.2 GHz for $Co_{85}Nb_{12}Zr_3$. For the Co_{91}-rich composition studied here, the FMR frequency is expected to be higher, approaching 2.27 GHz, as reported for pure cobalt at zero field [71].

Table 7
Numerically calculated skin depth δ and transverse permeability $|\mu_t|$ at 0.8 kA/m from the GMI curves for CoNbZr and CoNbZr/Au at 0.7 GHz and 1.4 GHz.

System	δ (0.7 GHz) nm	δ (1.4 GHz) nm	$\lvert\mu_t\rvert$ (0.7 GHz) 10^3	$\lvert\mu_t\rvert$ (1.4 GHz) 10^3
CoNbZr	145 ± 1	101 ± 1	3.6 ± 0.1	7.2 ± 0.1
CoNbZr/Au	102 ± 1	82 ± 1	8.8 ± 0.1	7.7 ± 0.1

The multilayer CoNbZr/Au system (Fig. 10(b)) shows a more complex GMI response. A double-peak structure is observed below 0.7 GHz, likely arising from the absence of a well-defined magnetic easy axis, as indicated by the similar hysteresis loops in both directions (Fig. 9). This lack of anisotropy leads to variable GMI behaviour, with the response alternating between single and double peaks below the FMR frequency, depending on minor variations in magnetisation during measurement. Above 0.7 GHz, the system transitions into the FMR regime, characterised by a broadening GMI response. The Au interlayers enhance the GMI ratio by approximately 50% and reduce the FMR frequency by nearly half compared to single-layer CoNbZr.

For the multilayer NiFe/Au system (Fig. 10(c)), a single peak is observed up to 0.5 GHz. At higher frequencies, the peak splits into a double feature due to ferromagnetic resonance (FMR), in agreement with previous studies on NiFe-based multilayers incorporating nonmagnetic metallic spacers [21,72]. The overall GMI response in the FMR regime closely resembles that of single-layer CoNbZr.

At 1.8 GHz, the GMI peaks occur at 1.6 kA/m for CoNbZr, 2.4 kA/m for CoNbZr/Au, and 3.2 kA/m for NiFe/Au, reflecting differences in magnetic anisotropy and FMR onset. To illustrate the field- and frequency-dependent evolution of the transverse permeability, $|\mu_t|$ was numerically calculated from Eq. (2) for selected applied fields, including zero as a reference. Fig. 11 presents $|\mu_t|$ as a function of frequency for these fields. At zero field, CoNbZr reaches a maximum roughly four times higher than CoNbZr/Au and half that of NiFe/Au. As the field increases, the peak shifts to higher frequencies, with CoNbZr/Au attaining 12 000 at 3.2 kA/m, about 50% above CoNbZr but still half of the NiFe/Au peak at 22 000.

The enhancement of $|\mu_t|$ in the multilayer CoNbZr compared to the single-layer system aligns with previous reports in Ref. [14] and can be attributed to the Au interlayer. This structure mitigates the pure skin effect and leverages the magneto-inductive effect, with the nonmagnetic Au spacer enhancing the GMI ratios at moderate frequencies [13,49,73,74].

The skin depth values listed in Table 7 were extracted by numerically fitting the measured complex impedance spectra using the model Eq. (2), as detailed in the theory section of this manuscript. Specifically, the L-M method was applied to simultaneously fit the magnitude $|Z|$ and phase $\arg(Z)$ of the impedance at each frequency, enabling the estimation of the complex transverse permeability μ_t and the resulting skin depth δ (see Eq. (1)).

The reduced FMR frequency observed for CoNbZr/Au correlates with its smaller skin depth. At 0.7 GHz, CoNbZr/Au exhibits a skin depth of (102 ± 1) nm, significantly smaller than the (145 ± 1) nm measured for single-layer CoNbZr, as shown in Table 7. This decrease in skin depth is accompanied by an enhanced transverse permeability $|\mu_t|$ of $(8.8 \pm 0.1) \cdot 10^3$ for CoNbZr/Au, compared to $(3.6 \pm 0.1) \cdot 10^3$ for CoNbZr.

At 1.4 GHz, the skin depth of CoNbZr decreases to (101 ± 1) nm, while that of CoNbZr/Au reduces further to (82 ± 1) nm. At this frequency, the transverse permeabilities of both systems become comparable ($(7.2 \pm 0.1) \cdot 10^3$ for CoNbZr and $(7.7 \pm 0.1) \cdot 10^3$ for CoNbZr/Au).

These results suggest that the Au interlayer not only reduces the skin depth but also enhances the magnetic permeability at lower

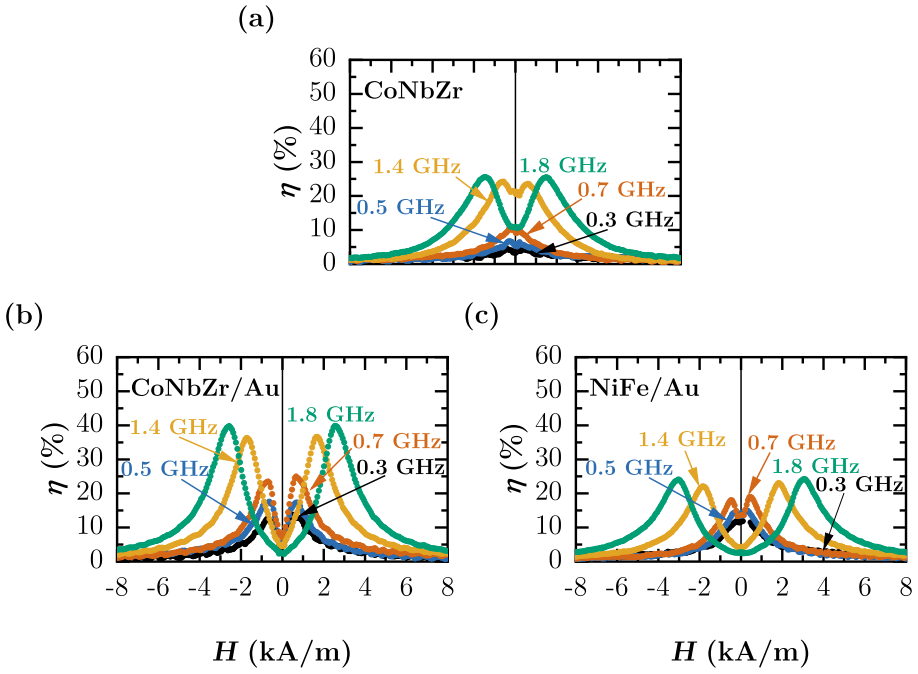

Fig. 10. GMI curves of 0.1 mm × 1 mm elements for (a) CoNbZr, (b) CoNbZr/Au, and (c) NiFe/Au. All systems show increasing GMI ratios with frequency. CoNbZr evolves from a single to a double peak above 0.3 GHz, with further broadening beyond 1.4 GHz due to FMR. CoNbZr/Au displays a double-peak response already at lower frequencies and an earlier FMR onset. NiFe/Au shows a single peak up to 0.5 GHz, followed by FMR-induced splitting.

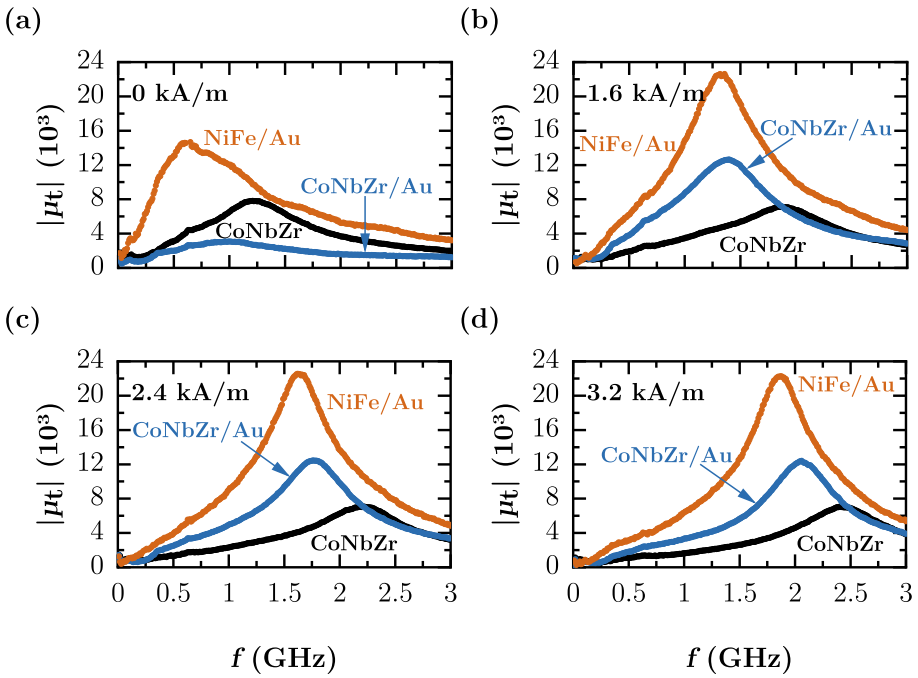

Fig. 11. Calculated absolute transverse permeability $|\mu_t|$ of 0.1 mm × 1 mm sputtered elements as a function of frequency f at different applied fields: (a) 0 kA/m, (b) 1.6 kA/m, (c) 2.4 kAm, and (d) 3.2 kA/m.

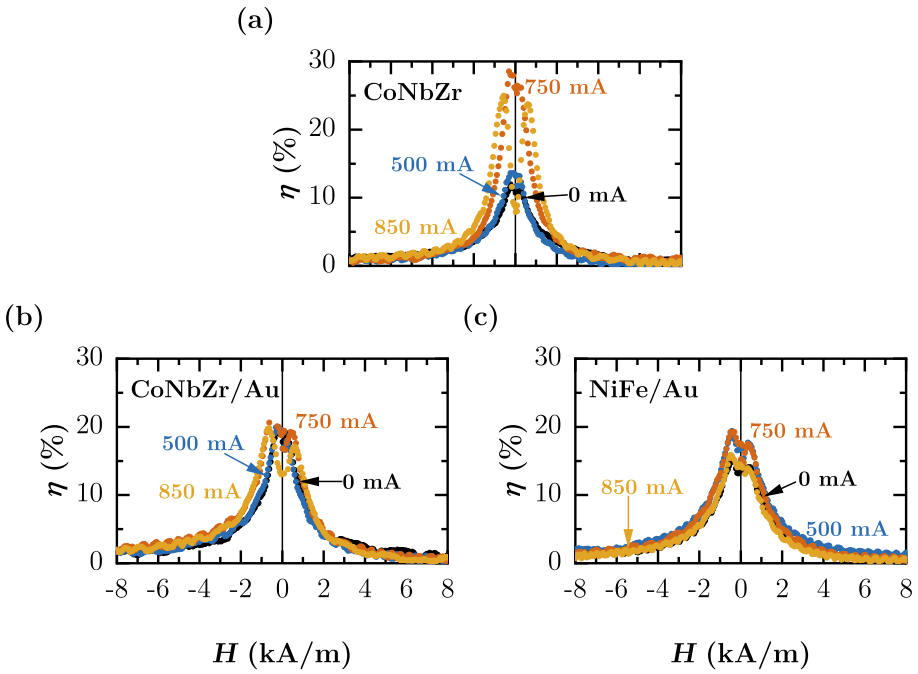

Fig. 12. GMI curves of 0.1 mm × 1 mm elements at 0.7 GHz as a function of annealing current for (a) CoNbZr, (b) CoNbZr/Au, and (c) NiFe/Au. In CoNbZr, η rises from 10% to nearly 30%, with a double peak appearing at 850 mA. CoNbZr/Au shows nearly constant η, while NiFe/Au exhibits FMR-induced double peaks with η ranging from 15% to 20%.

Table 8
Maximum GMI ratio, the magnetic field at which this maximum is reached, the slope of the GMI curve, and transverse permeability derived from the GMI curves (see Fig. 10) at a fixed frequency of 1.8 GHz.

System	η_{max} %	$H(\eta_{max})$ kA/m	s_{max} %/kAm^{-1}	$\lvert\mu_t\rvert$ 10^3
CoNbZr	26 ± 1	1.6 ± 0.1	18 ± 1	7.0 ± 0.1
CoNbZr/Au	40 ± 1	2.4 ± 0.1	33 ± 1	12.4 ± 0.1
NiFe/Au	24 ± 1	3.2 ± 0.1	19 ± 1	21.5 ± 0.1

frequencies, thereby contributing to the improved GMI response of the CoNbZr/Au multilayer. With CoNbZr approaching a skin depth of (101 ± 1) nm at 1.4 GHz and CoNbZr/Au reaching (102 ± 1) nm at 0.7 GHz, confirming their proximity to the FMR regime, in agreement with the peak broadening and splitting behaviour shown in Fig. 10(a) and (b).

Table 8 summarises the GMI characteristics at 1.8 GHz. CoNbZr/Au shows the highest maximum GMI ratio of 40% at (2.4 ± 0.1) kA/m and the highest sensitivity of (33 ± 1)%/kA m^{-1}, despite its transverse permeability being only half that of NiFe/Au. This is mainly due to its much higher resistivity, which is three times that of NiFe/Au (Table 4).

Comparing CoNbZr/Au with single-layer CoNbZr, although CoNbZr/Au exhibits a 1.7-fold lower resistivity compared to the single-layer CoNbZr, its 1.77-fold higher transverse permeability compensates for this, resulting in an overall enhanced GMI ratio. On the other hand, comparing single-layer CoNbZr with NiFe/Au, although CoNbZr exhibits a transverse permeability that is three times lower than that of NiFe/Au, its 4.5-fold higher resistivity compensates effectively, resulting in a higher GMI ratio.

4.4.2. Influence of annealing current

Fig. 12 shows the GMI curves of 0.1 mm × 1 mm structures, measured post-annealing over a magnetic field range of $H = \pm 8$ kA/m at 0.7 GHz, as a function of annealing current I. Results are presented for single-layer CoNbZr, multilayer CoNbZr/Au, and multilayer NiFe/Au.

For CoNbZr (Fig. 12(a)), the GMI ratio increases from 10% at I = 0 mA to nearly 30% at I = 750 mA, while at I = 850 mA a distinct double peak appears. In CoNbZr/Au (Fig. 12(b)), the GMI ratio remains nearly constant, though the double peak becomes more pronounced at I = 850 mA. NiFe/Au (Fig. 12(c)) shows a modest variation of η, increasing from 15% at I = 0 mA and I = 850 mA to 20% at I = 500 mA and I = 750 mA. The observed double peak in NiFe/Au originates from FMR.

The origin of the varying GMI curves in single-layer CoNbZr was investigated using MOKE images of the 0.1 mm × 1 mm structures after annealing at different currents (Fig. 13). At 0 mA (Fig. 13(a)), domains align along the longitudinal direction, indicated by bipolar contrast and white arrows, explaining the maximum GMI ratio at 0 kA/m (Fig. 12(a)). At 500 mA, domains rotate by approximately 60° relative to the width axis (Fig. 13(b)), leading to increased transverse permeability and reduced skin depth (Eq. (1)). At 750 mA, Fig. 13(c) reveals four grayscale levels indicating magnetisation directions, with the centre rotated by about 15° and edges aligned along the length. At 850 mA (Fig. 13(d)), the domain structure evolves into a horseshoe-like pattern with two distinct grayscale levels and a prominent central black band, markedly different from the lower-current states.

These domain variations affect stray fields: at 750 mA, magnetic flux forms closed loops due to a 15° rotation of magnetisation in the brightest and darkest areas, while intermediate contrast regions remain parallel, minimising stray fields. In contrast, the predominantly transverse magnetisation at 850 mA leads to open magnetic flux at domain ends, resulting in increased stray fields. Correspondingly, the GMI curves (Fig. 12(a)) reflect these changes: a double peak emerges at 750 mA as maxima shift away from 0 kA/m, becoming fully pronounced at 850 mA due to transverse easy-axis alignment. However, open flux at 850 mA reduces the GMI ratio compared to 750 mA.

The domain rotation observed up to 500 mA matches Kikuchi et al. [30] for Joule-heated CoNbZr films (40 μm × 2000 μm), who found no significant domain changes below 90 mA, but a gradual tilt from longitudinal towards the width direction up to 60° at 100 mA, and about 30° at the maximum current studied (120 mA). In contrast, the higher annealing currents (750 mA and 850 mA) used here induce more complex domain configurations, including horseshoe patterns with central alignment (Fig. 13(c,d)), likely due to differences in aspect ratio

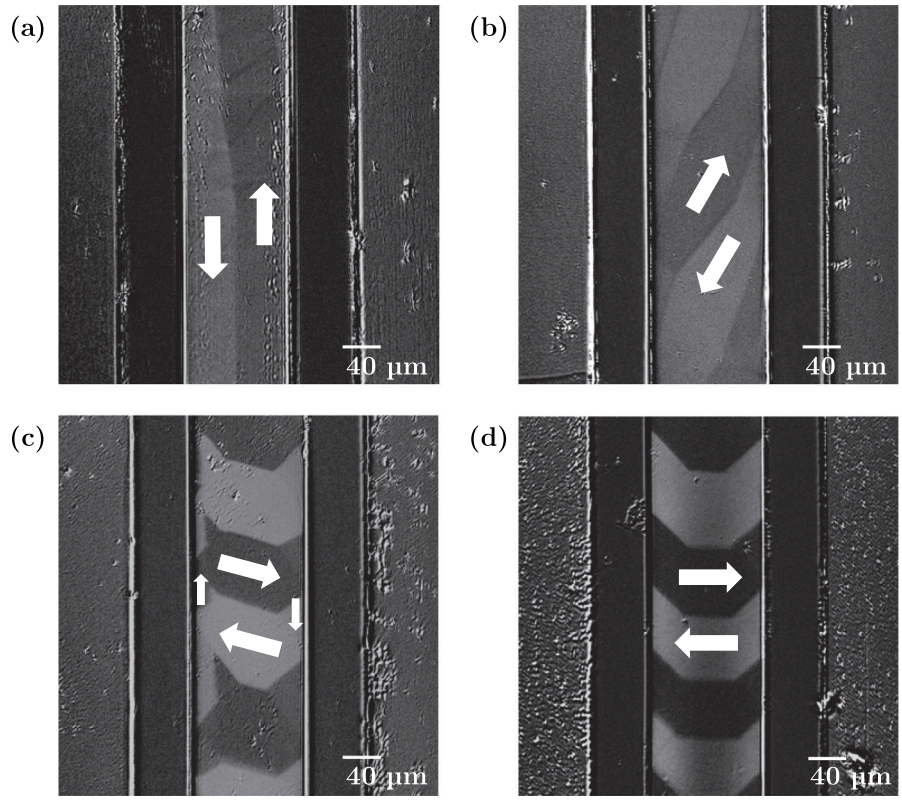

Fig. 13. MOKE images of 0.1 mm × 1 mm single-layer CoNbZr structures at annealing currents of (a) 0 mA, (b) 500 mA, (c) 750 mA, and (d) 850 mA. Domain orientation evolves from longitudinal alignment at 0 mA, to rotated states at 500 mA and 750 mA, and finally to a transverse horseshoe-like pattern with a central black band at 850 mA.

(100 µm × 1000 µm) and elevated current. This extended domain evolution underscores the key role of Joule heating in tailoring magnetic anisotropy and modulating the magnetoimpedance response in CoNbZr thin films.

4.4.3. Influence of lateral aspect ratio

Fig. 14 shows the GMI response as a function of the lateral aspect ratio for (a,b) single-layer CoNbZr, (c,d) multilayer CoNbZr/Au, and (e,f) multilayer NiFe/Au. Measurements were performed at 1.8 GHz over a magnetic field range of $H = \pm 8$ kA/m. Panels (a,c,e) depict the width dependence at fixed length (1 mm), while panels (b,d,f) illustrate length dependence at fixed width (20 µm).

Across all systems (a,c,e), the maximum GMI ratio is observed for widths between 10 µm and 20 µm. As the width decreases, the magnetic field corresponding to the double-peak maxima shifts towards lower values. The incorporation of an Au interlayer in the multilayer CoNbZr/Au system enhances the GMI ratio by 50% compared to single-layer CoNbZr. By contrast, the multilayer NiFe/Au system exhibits a slightly lower GMI ratio than CoNbZr/Au.

In panels (b,d,f), increasing the element length from 0.5 mm to 5 mm significantly enhances the GMI ratio across all systems. Single-layer CoNbZr (b) shows a fivefold increase, reaching a peak value of (180 ± 1)%. The multilayer CoNbZr/Au system (d) exhibits an even greater enhancement, with the GMI ratio increasing by a factor of 7.5 to (300 ± 1)%. Similarly, the multilayer NiFe/Au system (f) exhibits a fourfold increase, reaching (280 ± 1)%. The maximum GMI ratio for NiFe/Au occurs at an applied field of approximately 3.2 kA/m, which is approximately twice the field required for CoNbZr/Au. Across all systems, the increasing element length causes a slight shift in the GMI peak position.

Table 9 presents the maximum sensitivity values obtained from the GMI curves as a function of element width and length at a fixed frequency of 1.8 GHz. The highest sensitivity is found at a width of 20 µm,

Table 9
Maximum sensitivity extracted from the GMI curves as a function of element width and length at a fixed frequency of 1.8 GHz.

Sensitivity (%/kAm^{-1})	CoNbZr	CoNbZr/Au	NiFe/Au
1000:100	18 ± 1	33 ± 1	19 ± 1
1000:50	26 ± 1	46 ± 1	30 ± 1
500:20	26 ± 1	23 ± 1	39 ± 1
1000:20	39 ± 1	70 ± 1	54 ± 1
2000:20	76 ± 1	85 ± 1	85 ± 1
1000:10	31 ± 1	68 ± 1	41 ± 1
1000:5	24 ± 1	28 ± 1	28 ± 1
5000:20	169 ± 1	249 ± 1	183 ± 1

reaching (76 ± 1)%/kA m^{-1} for single-layer CoNbZr and (85 ± 1)%/kA m^{-1} for multilayer CoNbZr/Au and NiFe/Au at a fixed length of 1 mm. Incorporating the Au interlayer increases the sensitivity of the CoNbZr/Au multilayer by about 12% compared with single-layer CoNbZr.

As the element length increases while maintaining a fixed width of 20 µm, the sensitivity exhibits further enhancements. Single-layer CoNbZr reaches a maximum sensitivity of (169 ± 1)%/kA m^{-1}, an increase by a factor of 6.5. Similarly, multilayer CoNbZr/Au exhibits the strongest enhancement, with sensitivity increasing elevenfold to (249 ± 1)%/kA m^{-1}. In comparison, multilayer NiFe/Au achieves a sensitivity increase fivefold, reaching up to (183 ± 1)%/kA m^{-1}.

4.5. Discussion

This section discusses the key experimental findings, focusing on magnetic anisotropy and reversal mechanisms, resonance field variations, thermal effects, magnetic domain reconfiguration, and the influence of lateral aspect ratio.

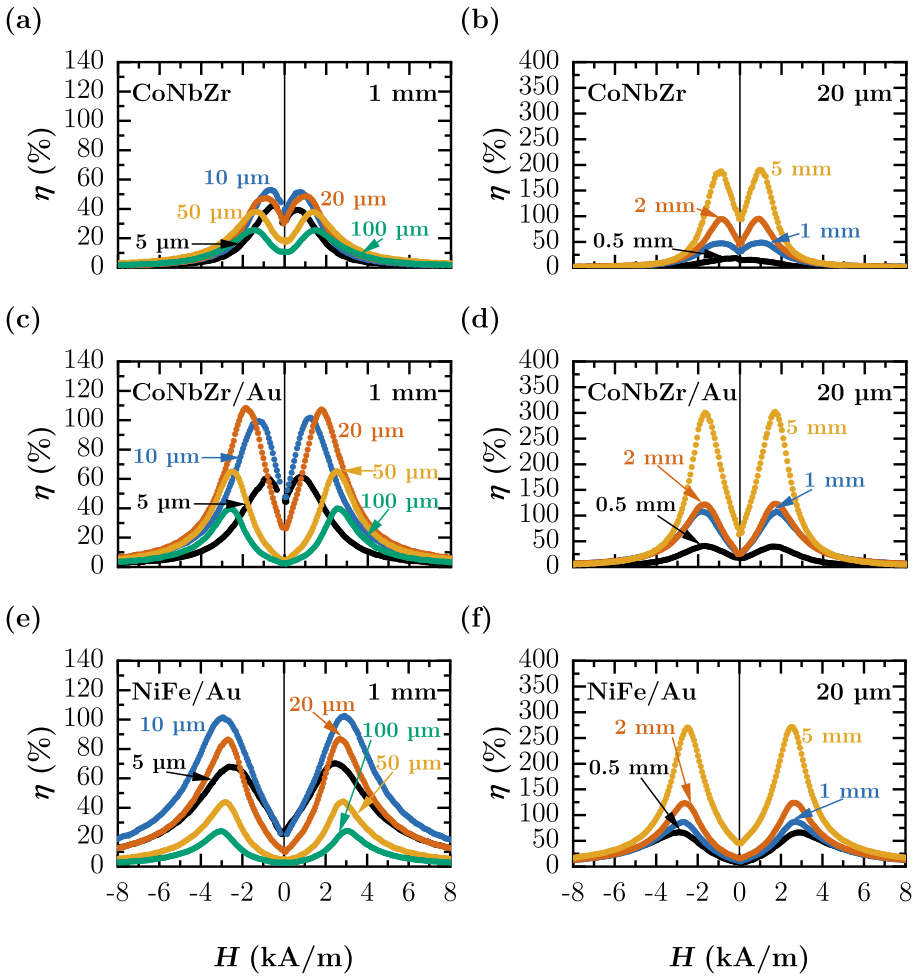

Fig. 14. GMI ratios η at 1.8 GHz for single-layer CoNbZr (a,b), CoNbZr/Au (c,d), and NiFe/Au (e,f). Panels (a,c,e) show η versus width (fixed length 1 mm), peaking between 10 µm and 20 µm. Panels (b,d,f) show η versus length (fixed width 20 µm), with multilayers exhibiting higher GMI than the single-layer.

4.5.1. Magnetic anisotropy and reversal mechanisms

For multilayer CoNbZr/Au (Fig. 9), no clear magnetic easy axis is observed, as hysteresis loops for length and width directions are similar. A possible explanation is an antiparallel alignment of adjacent ferromagnetic layers caused by magnetostatic stray-field coupling at the layer edges, as also reported for patterned NiFe/Ag multilayers where edge-induced magnetostatic interactions lead to such antiparallel alignment of the layers [75]. As a consequence, the external stray field is suppressed, and the elongated element shape no longer induces a significant shape anisotropy. The smooth CoNbZr/Au interfaces observed in Fig. 8(e) suggest that interface-driven exchange effects are weak, which further supports this interpretation. Nevertheless, other magnetostatic interactions across the multilayer stack cannot be excluded.

In contrast, the hysteresis loops of multilayer NiFe/Au differ significantly for the length and width directions, indicating that shape anisotropy plays a more prominent role. Here, exchange coupling between adjacent crystalline NiFe layers may dominate, leading to antiparallel magnetisation alignment (see Fig. 8(h)). The difference between the two systems thus likely originates from their structural nature.

Steps in the length-direction hysteresis loops of CoNbZr/Au and NiFe/Au indicate that at least one layer reverses at a different field, likely due to interlayer interactions or local property variations from thickness fluctuations or deposition conditions, as shown in Fig. 9(a). In CoNbZr/Au, minimal interdiffusion suggests that such differences stem from local anisotropy variations or patterning-induced effects (edge roughness, sidewall deposition). In NiFe/Au, grain size variations in NiFe may cause similar behaviour. In single-layer CoNbZr, similar steps are attributed to inhomogeneities, stress-induced anisotropies, or magnetoelastic effects.

4.5.2. Resonance field variations

GMI curves at 1.8 GHz (Fig. 10) exhibit double peaks at 1.6 kA/m for CoNbZr, 2.4 kA/m for CoNbZr/Au, and 3.2 kA/m for NiFe/Au. According to Eq. (4), the peak position depends on the saturation magnetisation M_s. As a result, CoNbZr with its higher M_s reaches resonance at a lower field than CoNbZr/Au and NiFe/Au (Table 6).

In the FMR regime, interfacial exchange coupling in multilayers adds anisotropy terms that modify the effective field. TEM images show sharp CoNbZr/Au interfaces and granular NiFe/Au structures, suggesting interfacial strain or roughness as additional anisotropy sources. Differences in damping and gyromagnetic ratio further influence resonance. Combined, these effects may explain the observed shifts.

4.5.3. Thermal effects and magnetic domain reconfiguration

The pronounced double peak in CoNbZr/Au at 850 mA and 0.7 GHz shown in Fig. 12(b) results from current-induced heating. This relieves stresses and promotes favourable domain alignment, enhancing resonance. In NiFe/Au (see Fig. 12(c)), heating similarly increases the GMI ratio by reducing stress and benefiting from the higher transverse permeability. The drop at 850 mA indicates that excessive heating reduces transverse permeability.

Horseshoe-like domains at 850 mA (Fig. 13(d)) likely arise from annealing-induced anisotropy or strain changes. The central black band

may indicate reduced magnetisation or flux closure. Micromagnetic simulations or further experiments are required to confirm these interpretations.

4.5.4. Lateral aspect ratio

The GMI peak shift with fixed geometry (Fig. 14) is mainly linked to M_s variations affecting H_K (Eq. (4)). Lateral aspect ratio modifies effective demagnetising fields, influenced by interfacial coupling, intrinsic properties, and local anisotropies from strain or roughness (Fig. 8).

As Table 1 shows, decreasing width increases N_y and decreases N_x, thereby increasing K_s (Eq. (12)). Consequently, the easy axis aligns along the sample's length, enhancing microwave absorption at resonance and increasing the GMI ratio. However, for widths <10 μm, edge effects distort domains and reduce GMI despite higher demagnetising fields along the sample's width. Similar observations of edge effects on GMI behaviour in thin films have been reported previously [76]. Increasing length reduces N_x and enlarges the oscillating magnetic moment volume, lowering the field required for resonance and enhancing GMI performance.

5. Conclusion

This study investigated CoNbZr thin films and CoNbZr/Au and NiFe/Au multilayers as candidates for GHz-range magnetic sensors. CoNbZr was chosen for its remarkable ability to remain amorphous even at high film thicknesses. TEM diffraction patterns confirmed that both single-layer CoNbZr and CoNbZr/Au multilayers retain an amorphous structure, in contrast to crystalline NiFe/Au. Compositional analysis revealed deviations from the target, with the Co/Nb ratio in sputtered CoNbZr increasing from 7 to 11.

Electric characterisation showed that CoNbZr/Au multilayers have resistivities roughly three times higher than NiFe/Au and half that of single-layer CoNbZr, highlighting the influence of Au interlayers on electron transport. In-plane hysteresis loops yielded saturation magnetisations of (1.01 ± 0.05) MA/m for CoNbZr, (0.85 ± 0.04) MA/m for CoNbZr/Au, and (0.68 ± 0.03) MA/m for NiFe/Au. A simple dilution model accurately predicts saturation magnetisation for all systems and resistivity for NiFe/Au, while overestimating CoNbZr/Au resistivity by 55%, indicating additional scattering mechanisms.

GMI measurements highlight the advantages of CoNbZr/Au for sensing applications. The incorporation of Au interlayers increases the GMI ratio by 50% and halves the FMR frequency compared with single-layer CoNbZr. Joule-heating experiments on $100\,\mu m \times 1000\,\mu m$ strips show an almost threefold increase in GMI for single-layer CoNbZr, whereas multilayers remain largely unchanged.

At 1.8 GHz, the highest GMI performance was observed in a $20\,\mu m \times 5000\,\mu m$ CoNbZr/Au strip, reaching 300% with a sensitivity of 249%/kA m^{-1}. Under identical conditions, single-layer CoNbZr and NiFe/Au reached lower values of 180% (169%/kA m^{-1}) and 280% (183%/kA m^{-1}), respectively. The superior response of CoNbZr/Au is primarily attributed to differences in in-plane demagnetising factors and saturation magnetisations.

While these findings confirm the promise of CoNbZr/Au multilayers, they reflect a specific optimised configuration. Future work should explore alternative interlayer materials such as Ti or Cu to balance performance and cost, optimise layer thicknesses, apply transverse magnetic bias during sputtering, and integrate thicker conductive non-ferromagnetic layers to improve current distribution. The demonstrated effect of current annealing on single-layer CoNbZr also highlights a scalable route for performance enhancement.

Overall, this study demonstrates that CoNbZr/Au multilayers combine the microstructural stability of amorphous alloys with the tunable electric and magnetic properties afforded by interlayers, establishing them as a highly promising platform for resonant GHz-range magnetic sensors.

CRediT authorship contribution statement

Indujan Sivanesarajah: Writing – review & editing, Writing – original draft, Visualization, Validation, Methodology, Investigation, Formal analysis, Data curation, Conceptualization. **Leon Abelmann:** Writing – review & editing, Supervision, Resources, Formal analysis. **Uwe Hartmann:** Writing – review & editing, Supervision, Resources, Project administration, Funding acquisition.

Declaration of Generative AI and AI-assisted technologies in the writing process

During the preparation of this work, the authors used ChatGPT to improve the readability, language, grammar, spelling, and style of the manuscript. After using this tool, the authors reviewed and edited the content as needed and take full responsibility for the content of the publication.

Declaration of competing interest

The authors declare that they have no known competing financial interests or personal relationships that could have appeared to influence the work reported in this paper.

Acknowledgements

The project was conducted at Saarland University as part of the BMBF-funded collaborative research initiative "ForMikro-spinGMI".

The authors thank Christoph Pauly and Christian Schäfer from the Chair of Functional Materials for preparing the TEM lamellae by FIB milling. We further thank Jörg Schmauch from INM Saarbrücken for his support in collecting the TEM, SEM, and EDX data presented in this paper. Additional thanks go to Björn Heinz and Philipp Schwenke (RPTU Kaiserslautern, Germany) for performing the VSM measurements, to Carsten Brill from KIST Europe for his assistance with film deposition, and to Gregor Büttel for his valuable contributions throughout the project.

Data availability

Data will be made available on request.

References

[1] L.V. Panina, K. Mohri, Appl. Phys. Lett. 65 (1994) 1189.
[2] R.S. Beach, A.E. Berkowitz, Appl. Phys. Lett. 64 (1994) 3652.
[3] Y. Nishibe, H. Yamadera, N. Ohta, K. Tsukada, Y. Nonomura, Sensors Actuators A 82 (2000) 155.
[4] K. Mohri, T. Uchiyama, L.V. Panina, M. Yamamoto, K. Bushida, J. Sens. 2015 (2015) 1.
[5] M.A. Khan, J. Sun, B. Li, A. Przybysz, J. Kosel, Eng. Res. Express 3 (2021) 022005.
[6] G.V. Kurlyandskaya, M.L. Sánchez, B. Hernando, V.M. Prida, P. Gorria, M. Tejedor, Appl. Phys. Lett. 82 (2003) 3053.
[7] T. Uchiyama, S. Nakayama, K. Mohri, K. Bushida, Phys. Status Solidi (A) Appl. Mater. Sci. 206 (2009) 639.
[8] T. Uchiyama, K. Mohri, S. Nakayama, IEEE Trans. Magn. 47 (2011) 3070.
[9] T. Uchiyama, T. Takiya, AIP Adv. 7 (2017) 056644.
[10] N.A. Buznikov, A.P. Safronov, I. Orue, E.V. Golubeva, V.N. Lepalovskij, A.V. Svalov, A.A. Chlenova, G.V. Kurlyandskaya, Biosens. Bioelectron. 117 (2018) 366.
[11] T. Nakai, Sensors 21 (2021) 4063.
[12] Y. Nishibe, N. Ohta, K. Tsukada, H. Yamadera, Y. Nonomura, K. Mohri, T. Uchiyama, IEEE Trans. Veh. Technol. 53 (2004) 1827.
[13] A. García-Arribas, E. Fernández, D. de Cos, Thin-film magneto-impedance sensors, in: Magnetic Sensors - Development Trends and Applications, InTech, 2017, pp. 39–62.
[14] H. Yokoyama, K. Kusunoki, Y. Hayashi, S. Hashi, K. Ishiyama, J. Magn. Magn. Mater. 478 (2019) 38.
[15] R.M. Bozorth, Ferromagnetism, David Van Nostrand Company, Inc., 1951.
[16] B. Cullity, C.D. Graham, Introduction to Magnetic Materials, Wiley, 2009.

[17] N. Saito, H. Fujiwara, Y. Sugita, J. Phys. Soc. Japan 19 (1964) 1116.
[18] E.F. Silva, M.A. Corrêa, R.D.D. Pace, C.C.P. Cid, P.R. Kern, M. Carara, C. Chesman, O.A. Santos, R.L. Rodríguez-Suárez, A. Azevedo, S.M. Rezende, F. Bohn, J. Phys. D: Appl. Phys. 50 (2017) 185001.
[19] S. Cheng, P. Lubitz, Y. Zheng, A. Edelstein, J. Magn. Magn. Mater. 282 (2004) 109.
[20] G.V. Kurlyandskaya, L. Elbaile, F. Alves, B. Ahamada, R. Barrué, A.V. Svalov, V.O. Vas'kovskiy, J. Phys. Condens. Matter 16 (2004) 6561.
[21] D. de Cos, V.N. Lepalovskij, G.V. Kurlyandskaya, A. García-Arribas, J.M. Barandiarán, J. Magn. Magn. Mater. 320 (2008) 954.
[22] M.A. Corrêa, F. Bohn, C. Chesman, R.B. da Silva, A.D.C. Viegas, R.L. Sommer, J. Phys. D: Appl. Phys. 43 (2010) 295004.
[23] G.V. Kurlyandskaya, A.V. Svalov, E. Fernandez, A. Garcia-Arribas, J.M. Barandiaran, J. Appl. Phys. 107 (2010) 09C502.
[24] A.V. Svalov, E. Fernandez, A. Garcia-Arribas, J. Alonso, M.L. Fdez-Gubieda, G.V. Kurlyandskaya, Appl. Phys. Lett. 100 (2012) 1.
[25] V.O. Vas'kovskii, P.A. Savin, S.O. Volchkov, V.N. Lepalovskii, D.A. Bukreev, A.A. Buchkevich, Tech. Phys. 58 (2013) 105.
[26] H. Kikuchi, Y. Takahashi, K. Takahashi, T. Nakai, S. Hashi, K. Ishiyama, J. Appl. Phys. 115 (2014) 14.
[27] H. Kikuchi, S. Kamata, S. Oe, T. Nakai, S. Hashi, K. Ishiyama, IEEE Trans. Magn. 51 (2015) 18.
[28] H. Kikuchi, S. Kamata, Y. Takahashi, T. Nakai, S. Hashi, K. Ishiyama, IEEE Trans. Magn. 51 (2015) 1.
[29] H. Kikuchi, M. Tanii, T. Umezaki, AIP Adv. 10 (2020) 015334.
[30] H. Kikuchi, A. Ueno, M. Tanii, IEEE Trans. Magn. 58 (2022) 1.
[31] H. Kikuchi, A. Ueno, M. Tanii, IEEE Trans. Magn. 59 (2023) 1.
[32] A. García-Arribas, E. Fernández, A.V. Svalov, G.V. Kurlyandskaya, A. Barrainkua, D. Navas, J.M. Barandiaran, Eur. Phys. J. B 86 (2013) 136.
[33] G.V. Kurlyandskaya, E. Fernández, A. García-Arribas, V.N. Lepalovsij, S.O. Volchkov, J. Alloys Compd. 615 (2015) S296.
[34] J.M. González, A. García-Arribas, S.V. Shcherbinin, V.N. Lepalovskij, J.M. Collantes, G.V. Kurlyandskaya, Meas.: J. Int. Meas. Confed. 126 (2018) 215.
[35] S.V. Komogortsev, I.G. Vazhenina, S.A. Kleshnina, R.S. Iskhakov, V.N. Lepalovskij, A.A. Pasynkova, A.V. Svalov, Sensors 22 (2022) 3324.
[36] W.J. Choe, T.D. Lee, C.H. Hwang, Y.S. Park, J. Magn. Soc. Jpn. 15 (1991) 131.
[37] M.A. Corrêa, A.D.C. Viegas, R.B. da Silva, A.M.H. de Andrade, R.L. Sommer, J. Appl. Phys. 101 (2007) 043905.
[38] M.A. Corrêa, F. Bohn, A.D.C. Viegas, A.M.H. de Andrade, L.F. Schelp, R.L. Sommer, J. Phys. D: Appl. Phys. 41 (2008) 175003.
[39] Y. Shimada, IEEE Trans. Magn. 22 (1986) 89.
[40] H. Fujimori, H. Morita, M. Yamamoto, J. Zhang, IEEE Trans. Magn. 22 (1986) 1101.
[41] B.A. Belyaev, N.M. Boev, A.V. Izotov, P.N. Solovev, Russian Phys. J. 64 (2021) 1160.
[42] W. Giurlani, P. Marcantelli, F. Benelli, D. Bottacci, F. Gambinossi, M. Passaponti, A.D. Luca, E. Salvietti, M. Innocenti, Coatings 9 (2019) 405.
[43] A. Sommerfeld, Electrodynamics, Academic Press, 1952.
[44] L.D. Landau, E.M. Lifshitz, Electrodynamics of Continuous Media, Pergamon Press, 1984.
[45] D.X. Chen, J.L. Munoz, IEEE Trans. Magn. 35 (1999) 1906.
[46] M. Phan, H. Peng, Prog. Mater. Sci. 53 (2008) 323.
[47] K. Levenberg, Quart. Appl. Math. 2 (1944) 164.
[48] D.W. Marquardt, J. Soc. Ind. Appl. Math. 11 (1963) 431.
[49] K. Mohri, T. Kohsawa, K. Kawashima, H. Yoshida, L. Panina, IEEE Trans. Magn. 28 (1992) 3150.
[50] Y.-Y. Chen, J.-Y. Juang, Meas. Sci. Technol. 27 (2016) 074006.
[51] J.A. Osborn, Phys. Rev. 67 (1945) 351.
[52] A. Aharoni, J. Appl. Phys. 83 (1998) 3432.
[53] D.-X. Chen, E. Pardo, A. Sanchez, IEEE Trans. Magn. 41 (2005) 2077.
[54] J. Siegel, O. Lyutakov, V. Rybka, Z. Kolská, V. Švorčík, Nanoscale Res. Lett. 6 (2011) 96.
[55] D. Tomus, H.P. Ng, Micron 44 (2013) 115.
[56] A.J. Manuel, J.M.P.S. Quinton, Proc. R. Soc. Lond. Ser. A Math. Phys. Sci. 273 (1963) 412.
[57] E. Fernández, A. Lopez, A. García-Arribas, A.V. Svalov, G.V. Kurlyandskaya, A. Barrainkua, IEEE Trans. Magn. 51 (2015) 1.
[58] T.E. Kolding, IEEE Trans. Electron Devices 47 (2000) 734.
[59] J. Aguilera, R. Berenguer, Design and Test of Integrated Inductors for RF Applications, first ed., Kluwer Academic Publishers, 2003.
[60] H. Kikuchi, Y. Urakawa, M. Tanii, J. Magn. Magn. Mater. 539 (2021) 168356.
[61] N.W. Ashcroft, N.D. Mermin, Solid State Physics, Saunders College Publishing, 1976.
[62] R.J. Wakelin, E.L. Yates, Proc. Phys. Soc. Sect. B 66 (1953) 221.
[63] M. Yamaguchi, S. Tanaka, Y. Endo, S. Muroga, M. Nagata, 2015 Asia-Pacific Symposium on Electromagnetic Compatibility, APEMC, IEEE, 2015, pp. 536–539.
[64] E. Klokholm, J.A. Aboaf, J. Appl. Phys. 52 (1981) 2474.
[65] J. Neidhardt, S. Mráz, J.M. Schneider, E. Strub, W. Bohne, B. Liedke, W. Möller, C. Mitterer, J. Appl. Phys. 104 (2008) 063304.
[66] Y. Ochiai, K. Aso, M. Hayakawa, H. Matsuda, K. Hayashi, W. Ishikawa, Y. Iwasaki, J. Vac. Sci. Technol. A 4 (1986) 19.
[67] Y. Endo, T. Ito, T. Miyazaki, Y. Shimada, M. Yamaguchi, J. Appl. Phys. 117 (2015) 17A330.
[68] D. Gall, J. Appl. Phys. 119 (2016) 1.
[69] A. García-Arribas, E. Fernández, A. Svalov, G. Kurlyandskaya, J. Barandiaran, J. Magn. Magn. Mater. 400 (2016) 321.
[70] G. Nahrwold, J.M. Scholtyssek, S. Motl-Ziegler, O. Albrecht, U. Merkt, G. Meier, J. Appl. Phys. 108 (2010) 013907.
[71] H. Brömer, H. Huber, J. Magn. Magn. Mater. 8 (1978) 61.
[72] J.M. Barandiarán, A. García-Arribas, D.D. Cos, J. Appl. Phys. 99 (2006) 4.
[73] K. Hika, L. Panina, K. Mohri, IEEE Trans. Magn. 32 (1996) 4594.
[74] T. Morikawa, Y. Nishibe, H. Yamadera, Y. Nonomura, M. Takeuchi, Y. Taga, IEEE Trans. Magn. 33 (1997) 4367.
[75] T.L. Hylton, M.A. Parker, K.R. Coffey, J.K. Howard, R. Fontana, C. Tsang, Appl. Phys. Lett. 67 (1995) 1154.
[76] A. García-Arribas, J.M. Barandiarán, D. de Cos, J. Magn. Magn. Mater. 320 (2008) 5.